



Article

Facile Synthesis of Novel $\text{CaIn}_2\text{S}_4/\text{ZnIn}_2\text{S}_4$ Composites with Efficient Performance for Photocatalytic Reduction of Cr(VI) under Simulated Sunlight Irradiation

Siyu Xu ¹, Jun Dai ^{1,2}, Juan Yang ^{1,2,3,*} , Jun You ³ and Jingyi Hao ³

¹ Institute of Chemical Safety, School of Safety Science and Engineering, Henan Polytechnic University, Jiaozuo 454003, China; xusiyu2017@163.com (S.X.); daijun@hpu.edu.cn (J.D.)

² The Collaborative Innovation Center of Coal Safety Production of Henan, Henan Polytechnic University, Jiaozuo 454003, China

³ Institute of Applied Chemistry, College of Chemistry and Chemical Engineering, Henan Polytechnic University, Jiaozuo 454003, China; youjunhpu@163.com (J.Y.); haojingyi2018@163.com (J.H.)

* Correspondence: yangjuanhpu@163.com; Tel.: +86-391-398-7881

Received: 29 May 2018; Accepted: 25 June 2018; Published: 27 June 2018



Abstract: A series of novel and efficient heterostructured composites $\text{CaIn}_2\text{S}_4/\text{ZnIn}_2\text{S}_4$ have been synthesized using a facile hydrothermal method. XRD patterns indicate the as-prepared catalysts are two-phase composites of cubic phase CaIn_2S_4 and hexagonal phase ZnIn_2S_4 . FESEM (field emission scanning electron microscope) images display that the synthesized composites are composed of flower-like microspheres with wide diameter distribution. UV-Vis diffuse reflectance spectra (DRS) show that the optical absorption edges of the $\text{CaIn}_2\text{S}_4/\text{ZnIn}_2\text{S}_4$ composites shift toward longer wavelengths with the increase of the CaIn_2S_4 component. The photocatalytic activities of the as-synthesized composites are investigated by using the aqueous-phase Cr(VI) reduction under simulated sunlight irradiation. This is the first report on the application of the $\text{CaIn}_2\text{S}_4/\text{ZnIn}_2\text{S}_4$ composites as stable and efficient photocatalysts for the Cr(VI) reduction. The fabricated $\text{CaIn}_2\text{S}_4/\text{ZnIn}_2\text{S}_4$ composites possess higher photocatalytic performance in comparison with pristine CaIn_2S_4 or ZnIn_2S_4 . The $\text{CaIn}_2\text{S}_4/\text{ZnIn}_2\text{S}_4$ composite with a CaIn_2S_4 molar content of 30% exhibits the optimum photocatalytic activity. The primary reason for the significantly enhanced photoreduction activity is proved to be the substantially improved separation efficiency of photogenerated electrons/holes caused by forming the $\text{CaIn}_2\text{S}_4/\text{ZnIn}_2\text{S}_4$ heterostructured composites. The efficient charge separation can be evidenced by steady-state photoluminescence spectra (PLs) and transient photocurrent response. Based on the charge transfer between CaIn_2S_4 and ZnIn_2S_4 , an enhancement mechanism of photocatalytic activity and stability for the Cr(VI) reduction is proposed.

Keywords: $\text{CaIn}_2\text{S}_4/\text{ZnIn}_2\text{S}_4$ composites; Cr(VI); photocatalysis; simulated sunlight; hydrothermal method

1. Introduction

Semiconductor-based photocatalytic technology has exhibited great potential in green controlling of environmental contaminants and converting CO_2 to valuable chemicals [1–6]. However, the most studied photocatalysts (such as TiO_2 , ZnO , and ZnS) are active only under ultraviolet light irradiation. In view of the practical applications, visible light active photocatalysts with narrow bandgaps are greatly desirable. A great deal of research and efforts have been devoted to fabricating and synthesizing

visible-light-driven catalysts, [7–10]. For instance, visible-light photocatalysts based on metal sulfide, including the doped or functionalized ZnS [7,8], CdIn₂S₄ [9], ZnIn₂S₄ [10,11], CdIn₂S₄/ZnIn₂S₄ [12], and Cu₂ZnSnS₄ [13] have received broad attention in recent decades.

Among these metal sulfides, ZnIn₂S₄, as a ternary chalcogenide semiconductor possessing a narrow bandgap (2.34–2.48 eV), has aroused great interest in the field of visible-light-driven contaminants' degradation and hydrogen production by water splitting [10,11]. Although the studies have revealed that ZnIn₂S₄ has strong visible-light absorption, the catalytic activity of pristine ZnIn₂S₄ is lower than expected due to fast recombination of photogenerated charge carriers. Many efforts have been made to solve these drawbacks, including morphologies control, metal doping, and heterostructured composites construction [14–17]. The fabrication of heterojunction catalysts by coupling two kinds of semiconductor particles with a suitable energy band structure is identified as a valid method to promote photocatalytic activity because of the resulting effective separation of the photoinduced charge [18,19]. To improve the photocatalytic activity of pure ZnIn₂S₄, the heterojunction photocatalysts have been reported by hybridization with TiO₂, CdS, and C₃N₄ [20–22].

On the other hand, the metal sulfide semiconductors with narrow bandgaps generally undergo photocorrosion induced by the oxidative process of photogenerated holes, which result in poor photostability or deactivation during long-term recycling use under sunlight irradiation. For instance, CdS particles possess excellent catalytic activity, acceptable stability, and photocorrosion resistance under visible-light illumination, whereas the catalyst becomes unstable when exposed to sunlight irradiation [23]. As a visible-light photocatalyst, ZnIn₂S₄ also suffers from the critical drawback of high photocorrosion under sunlight illumination [24]. Very recently, Zhao et al. have synthesized chemically cross-linked ZnIn₂S₄/RGO heterostructured catalysts and investigated the sunlight-driven photocatalytic performance of 4-nitrophenol degradation. The experimental results demonstrate the as-fabricated ZnIn₂S₄/RGO possessed not only the enhanced visible-light catalytic performance but also prominently improved sunlight stability [24]. Therefore, to practically utilize sunlight-driven photocatalytic technology to control contaminants, the employed catalysts must be not only visible-light active but also stable when subjected to sunlight illumination.

CaIn₂S₄ is also an attractive ternary chalcogenide with a narrow bandgap (~1.9 eV) and meanwhile, is the cheapest alkaline earth metal-based semiconductor, which can serve as a potential visible-light catalyst. However, only a few of the investigations on the construction and synthesis of CaIn₂S₄-based composite photocatalysts have been reported to date [25–27]. Similar to other narrow-bandgap catalysts, the photocatalytic degradation efficiency of CaIn₂S₄ alone is very limited owing to the poor separation efficiency of photogenerated electrons and holes. By constructing the composite catalysts, such as CaIn₂S₄-RGO, CaIn₂S₄/g-C₃N₄, and CaIn₂S₄/TiO₂, the photocatalytic activity of CaIn₂S₄ has been significantly improved. For instance, direct Z-scheme CaIn₂S₄/TiO₂ catalysts with different CaIn₂S₄ weight percentages were prepared, and the photocatalytic performance of these composite catalysts was investigated by the degradation of isoniazid and metronidazole in the pharmaceutical wastewater. The improved catalytic performance can be ascribed to the significantly suppressed recombination of photoinduced charge carriers based on the Z-scheme charge transfer over CaIn₂S₄/TiO₂ catalysts. The aforementioned CaIn₂S₄-based composites show higher photocatalytic performance than the pure CaIn₂S₄ or TiO₂; nevertheless, the preparation processes are relatively complicated, and these composites cannot be obtained through one-step synthesis. Further research on the synthesis of the CaIn₂S₄-based composite photocatalysts by one-step hydrothermal methods is highly necessary to improve the photocatalytic activity of CaIn₂S₄.

Hexavalent Cr(VI) ions have been listed as one of the priority pollutants by the United States Environmental Protection Agency (US EPA) [28], due to the high toxicity, mutagenicity, and teratogenicity to the aquatic environment and human beings. The elimination of Cr(VI) ions have received increasing attention in the field of wastewater purification. The traditional techniques for removing Cr(VI) ions generally include precipitation, adsorption, ion-exchange, electro-coagulation [29], membrane separation, and photocatalytic reduction [30,31]. Considering solar

energy conversion, photocatalytic reduction is postulated to be an efficient and green technology for the elimination of Cr(VI) ions from contaminated water. The highly toxic Cr(VI) can be photoreduced to less harmful Cr(III) by means of a certain photocatalyst and reaction system.

In this study, flower-like $\text{CaIn}_2\text{S}_4/\text{ZnIn}_2\text{S}_4$ heterojunction composites are successfully synthesized by using a one-step hydrothermal method, and the photocatalytic performance of the Cr(VI) reduction is investigated under simulated sunlight illumination. To our knowledge, this is the first report about the $\text{CaIn}_2\text{S}_4/\text{ZnIn}_2\text{S}_4$ heterojunction composites for the photocatalytic reduction of Cr(VI). The heterojunction composites exhibit much higher reduction efficiency of Cr(VI) than the pure CaIn_2S_4 or ZnIn_2S_4 . Meanwhile, the $\text{CaIn}_2\text{S}_4/\text{ZnIn}_2\text{S}_4$ composites present excellent solar stability, and the photocorrosion of ZnIn_2S_4 is dramatically inhibited by constructing the $\text{CaIn}_2\text{S}_4/\text{ZnIn}_2\text{S}_4$ composites. The detailed mechanism of enhanced photocatalytic performance for the Cr(VI) reduction over the $\text{CaIn}_2\text{S}_4/\text{ZnIn}_2\text{S}_4$ composites is also proposed.

2. Materials and Methods

2.1. Materials

All the chemicals were of analytical grade and used as received without further purification. Calcium nitrate ($\text{Ca}(\text{NO}_3)_2$), zinc sulfate (ZnSO_4), indium chloride (InCl_3), thioacetamide (TAA), potassium dichromate, sulfuric acid (H_2SO_4), and ammonium oxalate were obtained from Aladdin Industrial Inc. (Shanghai, China). Diphenylcarbazide (DPC) was purchased from J & K Scientific Ltd. (Beijing, China). Double distilled water was used throughout this study.

2.2. Synthesis of Composite Photocatalysts

The $\text{CaIn}_2\text{S}_4/\text{ZnIn}_2\text{S}_4$ composite photocatalysts were prepared by hydrothermal route. Taking 20% $\text{CaIn}_2\text{S}_4/\text{ZnIn}_2\text{S}_4$ as an example, in a typical synthesis process, 0.2 mmol $\text{Ca}(\text{NO}_3)_2 \cdot 4\text{H}_2\text{O}$ and 0.8 mmol $\text{ZnSO}_4 \cdot 7\text{H}_2\text{O}$ were added into 40 mL of distilled water, followed by vigorous stirring for 30 min to form a clear solution. After that, 2 mmol $\text{InCl}_3 \cdot 4\text{H}_2\text{O}$ and 8 mmol TAA were put into the above-obtained mixed solution and stirred for additional 60 min at room temperature. The reaction mixture was then transferred into a Teflon-lined steel autoclave (Zhengxin Instrument, Yancheng, China), which was heated at 180 °C for 12 h. Finally, the obtained yellow solid was collected by filtration, washed with distilled water several times, and dried at 60 °C for 8 h. On that basis, different $\text{CaIn}_2\text{S}_4/\text{ZnIn}_2\text{S}_4$ composites with CaIn_2S_4 molar ratios of 5%, 10%, 20%, 30%, and 50% were synthesized and denoted as 5% $\text{CaIn}_2\text{S}_4/\text{ZnIn}_2\text{S}_4$, 10% $\text{CaIn}_2\text{S}_4/\text{ZnIn}_2\text{S}_4$, 20% $\text{CaIn}_2\text{S}_4/\text{ZnIn}_2\text{S}_4$, 30% $\text{CaIn}_2\text{S}_4/\text{ZnIn}_2\text{S}_4$, and 50% $\text{CaIn}_2\text{S}_4/\text{ZnIn}_2\text{S}_4$, respectively.

For comparison, the pure ZnIn_2S_4 was prepared by using a similar process without $\text{Ca}(\text{NO}_3)_2$. 1.0 mmol $\text{ZnSO}_4 \cdot 7\text{H}_2\text{O}$ was put into 40 mL of distilled water and stirred for 30 min. Then, 2 mmol $\text{InCl}_3 \cdot 4\text{H}_2\text{O}$ and 8 mmol TAA were added to the above-obtained solution and stirred for another 60 min. This mixture was subsequently transferred into a Teflon-lined steel autoclave and heated at 180 °C for 12 h. The precipitate was finally washed with deionized water and dried at 60 °C for 8 h to obtain pure ZnIn_2S_4 . For the preparation of the pure CaIn_2S_4 , 1.0 mmol $\text{Ca}(\text{NO}_3)_2 \cdot 4\text{H}_2\text{O}$ was added into 40 mL of distilled water and stirred for 30 min. After that, 2 mmol $\text{InCl}_3 \cdot 4\text{H}_2\text{O}$ and 8 mmol TAA were put into the above solution and then stirred for another 60 min. The obtained mixture was transferred into a Teflon-lined steel autoclave and heated at 180 °C for 12 h. The orange precipitate was finally washed with deionized water and dried at 60 °C for 8 h to obtain pure CaIn_2S_4 .

2.3. Material Characterization

The crystal structures of the as-prepared composites were investigated by using an X-ray diffractometer (XRD, Bruker D8 Advance, Karlsruhe, Germany), with Cu K α radiation ($\lambda = 0.15405$ nm). The morphologies of the synthesized samples were observed by a field emission scanning electron microscope (FEI, Quanta250, Hillsboro, OR, USA). The X-ray photoelectron

spectroscopy (XPS) experiment was carried out by using a Thermo Scientific ESCALAB 250xi system (Waltham, MA, USA), equipped with an Al anode. The BET (Brunauer-Emmett-Teller) surface areas of the composite samples were determined on a surface area analyzer (Autosorb-IQ, Quantachrome, Boynton Beach, FL, USA). UV–visible diffuse reflectance spectra (DRS) were collected on a Shimadzu UV-2550 spectrometer (Kyoto, Japan) using BaSO₄ as the reflectance standard. Photoluminescence spectra (PLs) were measured by using an Edinburgh FLS 980 fluorescence spectrometer (Livingston, UK), with a 330 nm excitation wavelength. The transient photocurrent measurement was performed on a CHI electrochemical workstation (CHI 760D, Shanghai, China) in the standard three-electrode system. Ag/AgCl electrode and a platinum wire were employed as the reference electrode and the counter electrode, respectively. The working electrodes were prepared according to our previous report [32]. The photocurrent was measured in the electrolyte of a 0.5 mol/L Na₂SO₄ aqueous solution (pH ~6.8) at a bias of +0.5 V. The light source was the same as that used in the photocatalytic experiments.

2.4. Photocatalytic Reduction of Cr(VI)

For the photocatalytic reduction of Cr(VI) under simulated sunlight irradiation, a 300 W xenon lamp (PLS-SXE 300, Perfect Light Co. Ltd., Beijing, China) was used as the light source. The incident light intensity was 75 mW/cm². In the typical photocatalytic test, 50 mg of photocatalyst was suspended in 50 mL of 20 mg/L Cr(VI) aqueous solution. After adding 5 mg of ammonium oxalate (a scavenger for photo-hole), the suspension was magnetically stirred in the dark for 30 min to establish an adsorption–desorption equilibrium. As the photocatalytic reduction proceeded, 3 mL of the reaction solution was taken out at a given time interval and centrifuged to remove the catalyst particles. The concentrations of Cr(VI) were determined colorimetrically at 540 nm using the diphenylcarbazide (DPC) method on a Shimadzu UV-160A UV–Vis spectrophotometer [33]. In addition, the total Cr ions concentrations were measured by an inductively coupled plasma-optical emission spectrophotometer (Agilent 725 ICP-OES, Palo Alto, CA, USA).

The apparent quantum efficiency (AQE) of Cr(VI) the photocatalytic reduction was measured under the same photocatalytic reaction conditions, except by using a 420 nm bandpass filter. The apparent quantum efficiencies were calculated according to the following equation:

$$\text{AQE}(\%) = \frac{\text{Number of reacted electrons}}{\text{Number of incident photons}} \times 100 = \frac{3 \times \text{number of reduced Cr(VI)}}{\text{Number of incident photons}} \times 100$$

$$\text{Number of incident photons} = \frac{I \times A \times t}{E(\lambda=420 \text{ nm})}$$

$$E(\lambda = 420 \text{ nm}) = \frac{h \times c}{\lambda}$$

where I , A , t , c , λ , and h are light intensity, light exposure area, irradiation time, light velocity, light wavelength, and Planck constant, respectively.

To evaluate the catalytic stability of the CaIn₂S₄/ZnIn₂S₄ composites, the photocatalysts—after the first run for the Cr(VI) reduction—were separated by centrifugation from the suspension and washed with 1 M nitrite acid solution and deionized water. After being dried at 60 °C, the recovered photocatalysts were reused for the next run of the photocatalytic Cr(VI) reductions under the same experimental conditions.

3. Results and Discussion

3.1. XRD Analysis and BET Surface Area

The phase composition and crystalline properties of the CaIn₂S₄/ZnIn₂S₄ composite samples were analyzed by XRD. Figure 1 displays the XRD patterns of the pure ZnIn₂S₄, CaIn₂S₄, and CaIn₂S₄/ZnIn₂S₄ composites. As indicated in Figure 1, the diffraction peaks of the pure ZnIn₂S₄ at $2\theta = 21.1^\circ$, 27.6° , 30.3° , 47.4° , 52.0° , and 55.6° corresponded to (006), (102), (104), (110), (116),

and (200) crystal planes of hexagonal phase ZnIn_2S_4 (JCPDS NO. 65-2023), respectively [24]. No other diffraction peaks were detected in the XRD pattern of ZnIn_2S_4 , indicating that the obtained ZnIn_2S_4 is highly pure. With the addition of $\text{Ca}(\text{NO}_3)_2$ in the preparation process, new diffraction peaks appeared in the XRD patterns, which belonged to the characteristic peaks of the cubic phase CaIn_2S_4 (JCPDS No. 16-0341) [25–27]. It can be also observed from Figure 1 that the intensity of the diffraction peaks belonging to the cubic CaIn_2S_4 phase increased gradually by increasing the mole proportion of CaIn_2S_4 , which indicated the existence of both CaIn_2S_4 and ZnIn_2S_4 in the as-synthesized composites. In addition, the diffraction peaks corresponding to binary sulfides, oxides, and other new compounds were not observed, indicating that CaIn_2S_4 and ZnIn_2S_4 maintained the pure phase and no impurities were formed in the obtained $\text{CaIn}_2\text{S}_4/\text{ZnIn}_2\text{S}_4$ composites.

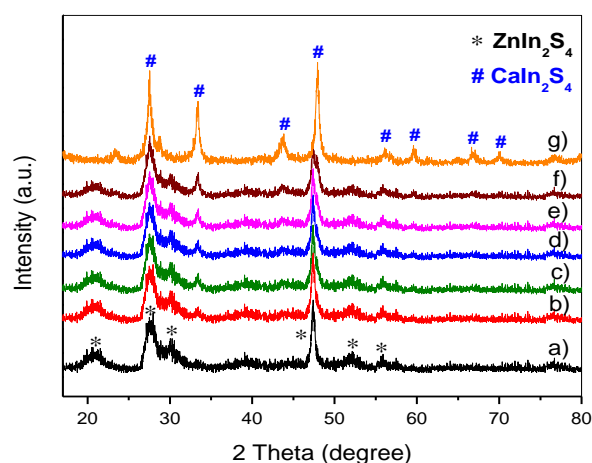


Figure 1. XRD patterns of pure ZnIn_2S_4 , CaIn_2S_4 , and $\text{CaIn}_2\text{S}_4/\text{ZnIn}_2\text{S}_4$ composites: (a) pure ZnIn_2S_4 , (b) 5% $\text{CaIn}_2\text{S}_4/\text{ZnIn}_2\text{S}_4$, (c) 10% $\text{CaIn}_2\text{S}_4/\text{ZnIn}_2\text{S}_4$, (d) 20% $\text{CaIn}_2\text{S}_4/\text{ZnIn}_2\text{S}_4$, (e) 30% $\text{CaIn}_2\text{S}_4/\text{ZnIn}_2\text{S}_4$, (f) 50% $\text{CaIn}_2\text{S}_4/\text{ZnIn}_2\text{S}_4$, and (g) pure CaIn_2S_4 .

The BET surface area of the pure ZnIn_2S_4 , CaIn_2S_4 , and $\text{CaIn}_2\text{S}_4/\text{ZnIn}_2\text{S}_4$ composites was measured, and the results are summarized in Table 1. As can be noted from Table 1, the specific surface area of the $\text{CaIn}_2\text{S}_4/\text{ZnIn}_2\text{S}_4$ composites decreased slightly with the continuous increment of CaIn_2S_4 component. The actual molar ratios of Ca–Zn in the $\text{CaIn}_2\text{S}_4/\text{ZnIn}_2\text{S}_4$ composites were determined by inductively coupled plasma elemental analysis, as presented in Table 1. It can be observed from Table 1 that the experimentally measured molar ratios of Ca–Zn in the synthesized composites were close to those of the added proportions in the preparation process.

Table 1. BET (Brunauer-Emmett-Teller) specific surface area, molar ratios of Ca–Zn in the synthesized $\text{CaIn}_2\text{S}_4/\text{ZnIn}_2\text{S}_4$ and apparent quantum efficiency (AQE) of the Cr(VI) reduction over these composites.

Samples	S_{BET} (m^2/g)	Molar Ratios of Ca:Zn (%)	AQE (%)
pure ZnIn_2S_4	59.2	0	3.7
5% $\text{CaIn}_2\text{S}_4/\text{ZnIn}_2\text{S}_4$	56.3	5.05	4.1
10% $\text{CaIn}_2\text{S}_4/\text{ZnIn}_2\text{S}_4$	54.7	9.67	4.5
20% $\text{CaIn}_2\text{S}_4/\text{ZnIn}_2\text{S}_4$	53.4	18.30	5.2
30% $\text{CaIn}_2\text{S}_4/\text{ZnIn}_2\text{S}_4$	52.1	26.52	6.6
50% $\text{CaIn}_2\text{S}_4/\text{ZnIn}_2\text{S}_4$	50.5	43.29	5.5
pure CaIn_2S_4	46.0	–	2.3

3.2. SEM and Elemental Mapping Analysis

The SEM images of the as-synthesized pure ZnIn_2S_4 , CaIn_2S_4 , and $\text{CaIn}_2\text{S}_4/\text{ZnIn}_2\text{S}_4$ composites are indicated in Figure 2. As can be observed from Figure 2, the pure ZnIn_2S_4 was composed of hierarchical microspheres with a wide distribution of diameter, which was consistent with the previous reports [17,24]. Introducing the Ca component had almost no influence on the morphologies of the $\text{CaIn}_2\text{S}_4/\text{ZnIn}_2\text{S}_4$ composites, which also exhibited flower-like microspheres constructed by numerous nanosheets in the form of random self-assembly. As a consequence, the porous structures with wide pore-size distribution could be expected. This would benefit the photocatalytic reaction by increasing the specific surface area. Moreover, the formation of the $\text{CaIn}_2\text{S}_4/\text{ZnIn}_2\text{S}_4$ heterojunction was evidenced by the elemental mapping of the as-synthesized composites (Figure 3). Maps of Zn–K, Ca–K, In–L, and S–K display the same shape and location, indicating the coexistence of ZnIn_2S_4 and CaIn_2S_4 components in the obtained composites. This provided solid evidence for the formation of $\text{CaIn}_2\text{S}_4/\text{ZnIn}_2\text{S}_4$ heterostructured composites.

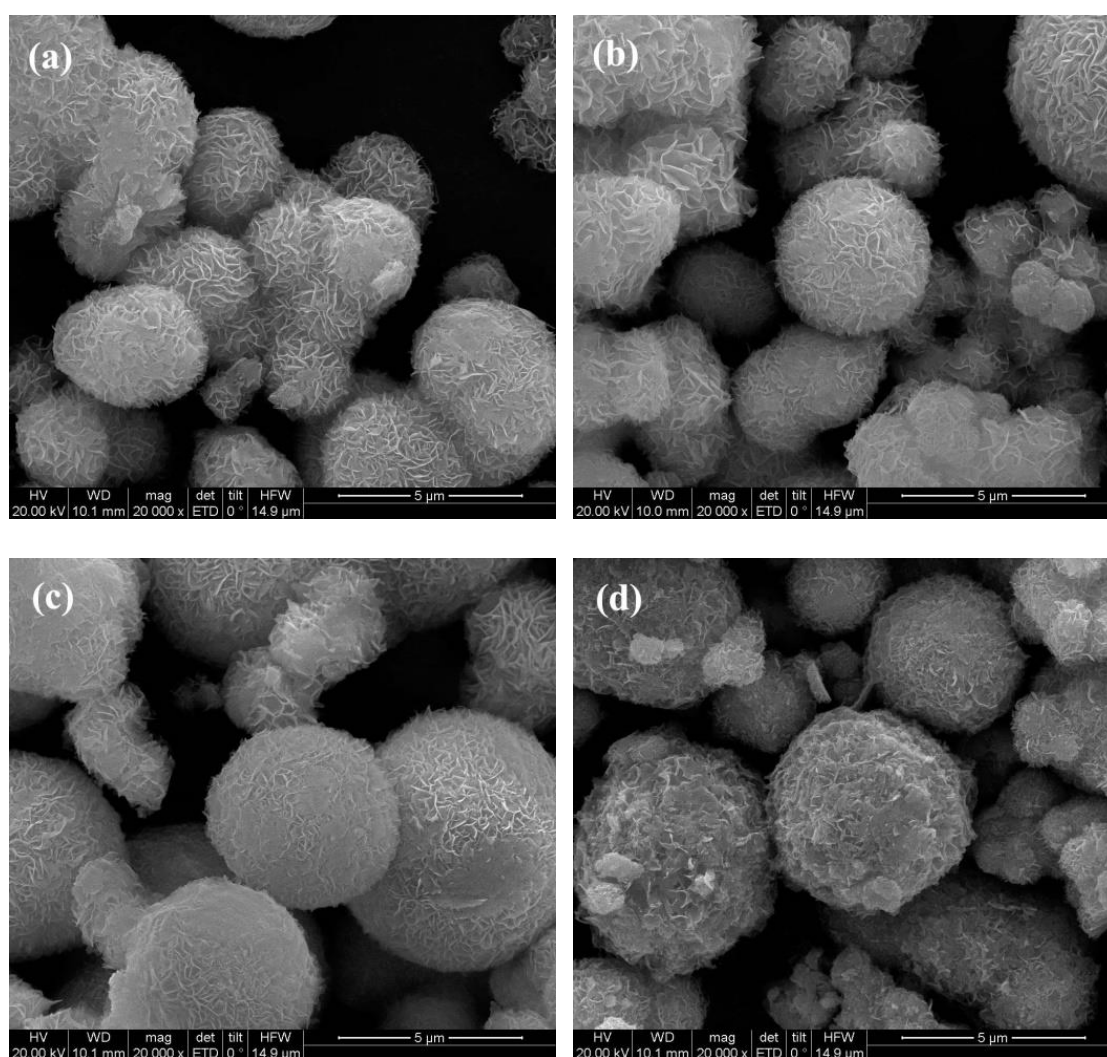


Figure 2. FE-SEM (field emission scanning electron microscope) images of (a) pure ZnIn_2S_4 , (b) 10% $\text{CaIn}_2\text{S}_4/\text{ZnIn}_2\text{S}_4$, (c) 30% $\text{CaIn}_2\text{S}_4/\text{ZnIn}_2\text{S}_4$, and (d) pure CaIn_2S_4 .

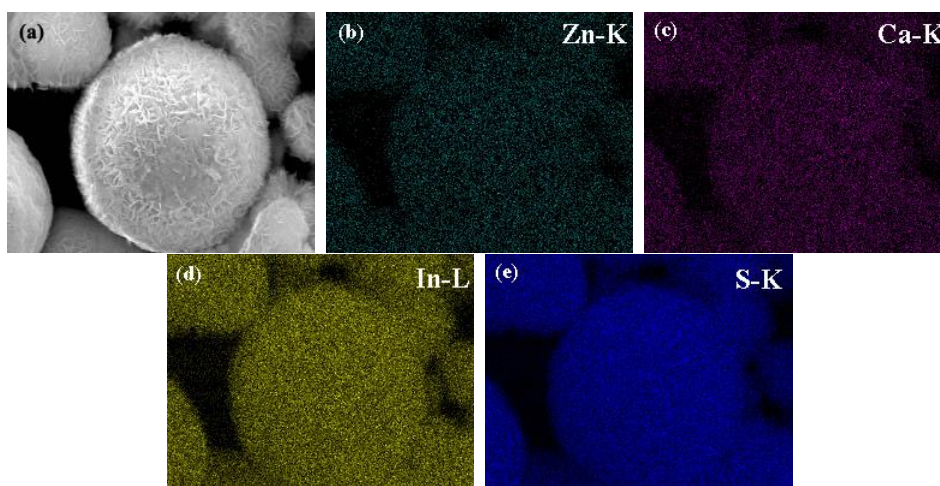


Figure 3. The EDS (Energy Dispersive Spectroscopy) elemental mapping images of the 30% $\text{CaIn}_2\text{S}_4/\text{ZnIn}_2\text{S}_4$ sample: (a) SEM image, (b) Zn-K, (c) Ca-K, (d) In-L, and (e) S-K, respectively.

3.3. XPS Analysis and Optical Properties

To determine the elemental composition and the corresponding chemical states of the synthesized composites, the XPS spectra of the 30% $\text{CaIn}_2\text{S}_4/\text{ZnIn}_2\text{S}_4$ sample are indicated in Figure 4. As can be seen from Figure 4a, the survey spectrum indicated the presence of Zn, Ca, In, and S elements in the 30% $\text{CaIn}_2\text{S}_4/\text{ZnIn}_2\text{S}_4$ sample. The high-resolution XPS spectrum for Zn is presented in Figure 4b. Two characteristic XPS signals were observed at binding energies of 1022.4 and 1045.3 eV, which were ascribed to $\text{Zn}^{2+} 2p_{1/2}$ and $\text{Zn}^{2+} 2p_{3/2}$, respectively [33,34]. The high-resolution XPS spectrum of In 3d is displayed in Figure 4c. The characteristic peaks centered at 444.7 and 452.3 eV can be attributed to the In $3d_{3/2}$ and In $3d_{5/2}$ signals of In^{3+} species, respectively [27,34]. In Figure 4d, the two peaks at the binding energies of 351.1 and 347.6 eV corresponded to the $2p_{3/2}$ and $2p_{1/2}$ levels of Ca^{2+} . Figure 4e shows an XPS signal centered at 162.5 eV, which can be assigned to the $2p_{1/2}$ level of S^{2-} in the as-prepared $\text{CaIn}_2\text{S}_4/\text{ZnIn}_2\text{S}_4$ composites [34]. These results further indicate that $\text{CaIn}_2\text{S}_4/\text{ZnIn}_2\text{S}_4$ composites can be successfully synthesized through a one-step hydrothermal reaction process.

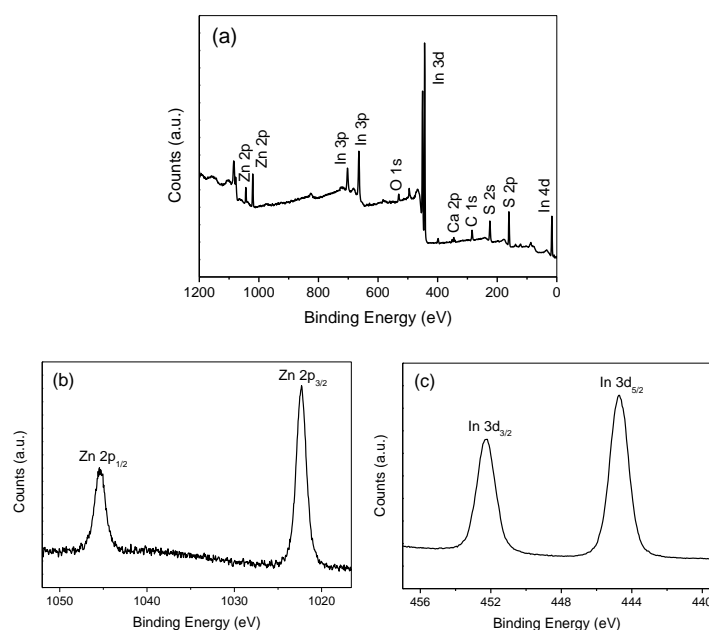


Figure 4. Cont.

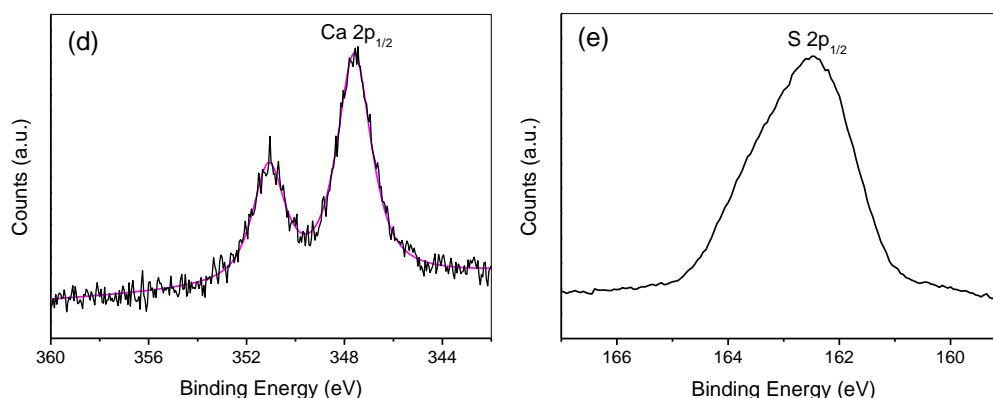


Figure 4. Typical XPS survey spectrum of 30% $\text{CaIn}_2\text{S}_4/\text{ZnIn}_2\text{S}_4$ (a), high-resolution XPS spectra of Zn 2p (b), In 3d (c), Ca 2p (d), and S 2p (e), respectively.

The optical absorption properties of the as-obtained $\text{CaIn}_2\text{S}_4/\text{ZnIn}_2\text{S}_4$ composites were analyzed by UV-Vis DRS, and the results are depicted in Figure 5a. The absorption edges of the pure ZnIn_2S_4 and CaIn_2S_4 samples were at around 537 nm and 638 nm, respectively. As can be also noted from Figure 5a, the absorption edges of the $\text{CaIn}_2\text{S}_4/\text{ZnIn}_2\text{S}_4$ samples were gradually red-shifted from 537 to 570 nm as the molar percentage of the CaIn_2S_4 component increased to 50%. The photoresponse of the $\text{CaIn}_2\text{S}_4/\text{ZnIn}_2\text{S}_4$ composites in visible-light region was significantly improved by comparison with that of the pure ZnIn_2S_4 . Moreover, the UV-Vis DRS shown in Figure 5a were all very steep, demonstrating the visible-light absorption was ascribed to the intrinsic band transition instead of the transition from impurity levels [35]. Based on the optical absorption theory of the bandgap semiconductor, the bandgap energy of the pure CaIn_2S_4 and ZnIn_2S_4 can be calculated by the Equation (1) [36] as follows:

$$\alpha h\nu = A (h\nu - E_g)^{n/2} \quad (1)$$

where α , ν , E_g , and A represent the absorption coefficient, light frequency, bandgap energy, and a constant, respectively. The value of n depends on the type of optical transition of a semiconductor ($n = 1$ for the direct transition and $n = 4$ for the indirect transition). According to the previous literature [27,37], ZnIn_2S_4 and CaIn_2S_4 are direct-transition semiconductors, and thus, the bandgap energies of CaIn_2S_4 and ZnIn_2S_4 can be estimated from the plots of $(\alpha h\nu)^2$ versus light energy ($h\nu$). As illustrated in Figure 5b, the estimated bandgaps were 2.03 and 2.43 eV for the pure CaIn_2S_4 and ZnIn_2S_4 , respectively, which matched well with the literature values [15,27]. For the composite catalysts, the photocatalytic performance was primarily determined by the valence band (VB) and conduction band (CB) energy levels of the constituent semiconductors. Based on the following equations, the VB and CB positions of the pristine ZnIn_2S_4 and CaIn_2S_4 can be obtained:

$$E_{\text{VB}} = \chi - E_e + 0.5 E_g \quad (2)$$

$$E_{\text{CB}} = E_{\text{VB}} - E_g \quad (3)$$

where E_{VB} and E_{CB} are the potential of the VB and CB edge, E_g is the bandgap energy, χ is the geometric mean of the absolute electronegativity of the constituent atoms in the semiconductor, and E_e is the energy of free electrons on the hydrogen scale with a value of 4.5 eV. The χ values of ZnIn_2S_4 and CaIn_2S_4 were 4.86 and 4.39 eV, respectively. Based on the above empirical equations, the E_{VB} values of ZnIn_2S_4 and CaIn_2S_4 were estimated to be +1.58 and +0.91 eV. The corresponding E_{CB} values were also calculated to be -0.85 and -1.12 eV, respectively.

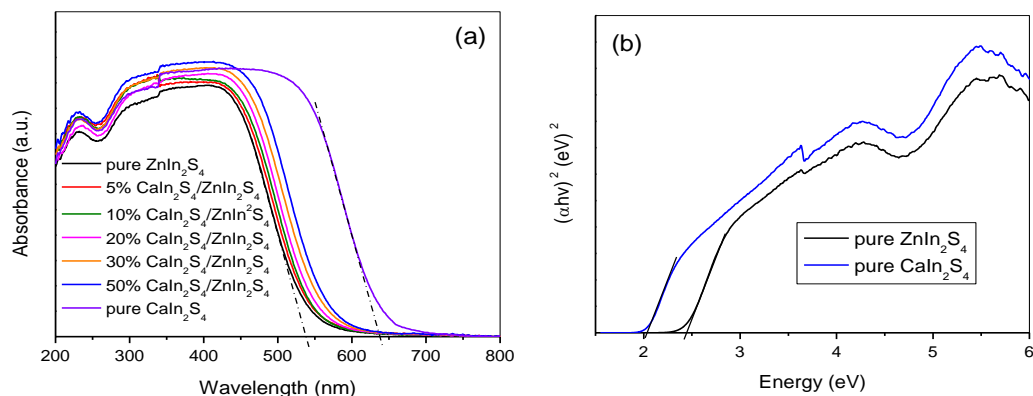


Figure 5. (a) UV-Vis DRS of the pure ZnIn_2S_4 , CaIn_2S_4 , and $\text{CaIn}_2\text{S}_4/\text{ZnIn}_2\text{S}_4$ composites, (b) Plots of $(\alpha h\nu)^2$ vs. light energy ($h\nu$) of the pure ZnIn_2S_4 and CaIn_2S_4 .

3.4. Photocatalytic Activity

The photocatalytic performances of the ZnIn_2S_4 , CaIn_2S_4 , and $\text{CaIn}_2\text{S}_4/\text{ZnIn}_2\text{S}_4$ composites were investigated by the aqueous-phase Cr(VI) reduction under simulated sunlight irradiation (Figure 6A). Cr(VI) cannot be reduced in the absence of light illumination or photocatalysts. The pure ZnIn_2S_4 displayed a relatively higher photocatalytic activity of the Cr(VI) reduction than the CaIn_2S_4 sample. About 42% of Cr(VI) was reduced over the pure CaIn_2S_4 , while ZnIn_2S_4 can reduce 63% of Cr(VI) after irradiation of 30 min. All the $\text{CaIn}_2\text{S}_4/\text{ZnIn}_2\text{S}_4$ composites exhibited higher photocatalytic efficiency than the pristine CaIn_2S_4 and ZnIn_2S_4 , indicating that the combination of CaIn_2S_4 and ZnIn_2S_4 can improve the photocatalytic reduction performance of these composites.

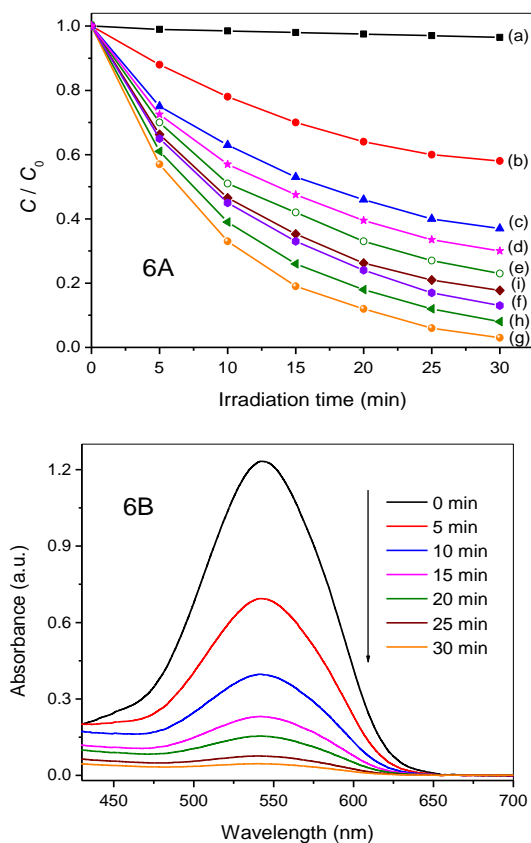


Figure 6. Cont.

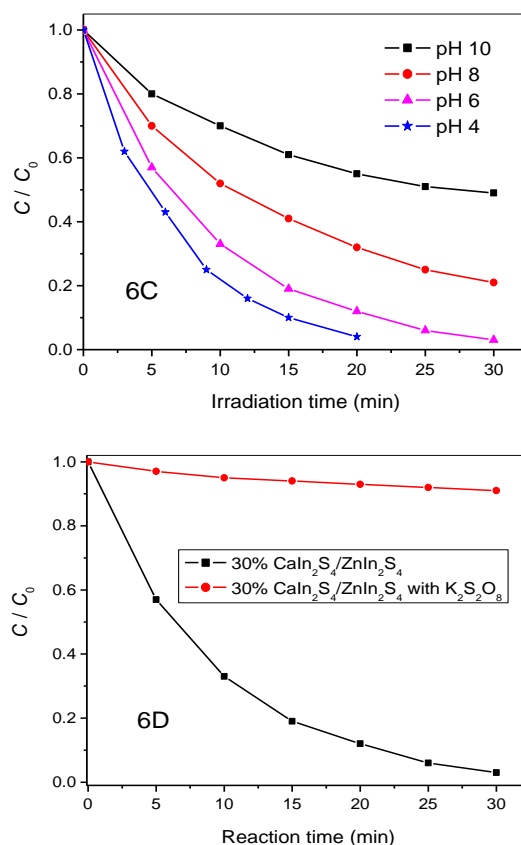


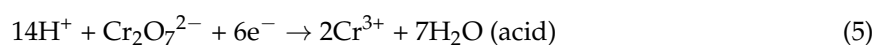
Figure 6. (A) Photocatalytic reduction of Cr(VI) as a function of irradiation time over different catalysts: (a) no catalyst, (b) pure CaIn_2S_4 , (c) pure ZnIn_2S_4 , (d) 5% $\text{CaIn}_2\text{S}_4/\text{ZnIn}_2\text{S}_4$, (e) 10% $\text{CaIn}_2\text{S}_4/\text{ZnIn}_2\text{S}_4$, (f) 20% $\text{CaIn}_2\text{S}_4/\text{ZnIn}_2\text{S}_4$, (g) 30% $\text{CaIn}_2\text{S}_4/\text{ZnIn}_2\text{S}_4$, (h) 50% $\text{CaIn}_2\text{S}_4/\text{ZnIn}_2\text{S}_4$, and (i) mechanically mixed 30% $\text{CaIn}_2\text{S}_4 + 70\%\text{ZnIn}_2\text{S}_4$; (B) time-dependent absorption spectral pattern of diphenylcarbazide (DPC)-Cr(VI) complex solutions after the reduction over 30% $\text{CaIn}_2\text{S}_4/\text{ZnIn}_2\text{S}_4$ (pH = 6); (C) photocatalytic reduction of Cr(VI) under different pH values over 30% $\text{CaIn}_2\text{S}_4/\text{ZnIn}_2\text{S}_4$; (D) the controlled experiment for photocatalytic reduction of Cr(VI) over the 30% $\text{CaIn}_2\text{S}_4/\text{ZnIn}_2\text{S}_4$ composites with the addition of $\text{K}_2\text{S}_2\text{O}_8$ (0.1 mmol) as a scavenger for photoinduced electrons.

For the synthesized $\text{CaIn}_2\text{S}_4/\text{ZnIn}_2\text{S}_4$ composite catalysts, the photocatalytic were closely associated with the contents of the CaIn_2S_4 component. As can be noted from Figure 6A, the photocatalytic activities of the $\text{CaIn}_2\text{S}_4/\text{ZnIn}_2\text{S}_4$ composite catalysts increased with the increment of component CaIn_2S_4 . The 30% $\text{CaIn}_2\text{S}_4/\text{ZnIn}_2\text{S}_4$ composite photocatalyst exhibited the highest activity for the Cr(VI) reduction, whereas the greater increase in the amount of CaIn_2S_4 resulted in a decrease in the Cr(VI) reduction rates. It can be ascribed to the low photocatalytic activity of the pure CaIn_2S_4 because of the slow separation of the photogenerated charge carriers. Moreover, the apparent quantum efficiencies (AQE) of the Cr(VI) photocatalytic reduction over the synthesized composites were also calculated, and the corresponding results are summarized in Table 1. As indicated in Table 1, the AQE of the 30% $\text{CaIn}_2\text{S}_4/\text{ZnIn}_2\text{S}_4$ nanocomposite catalyst reached 6.6%, which presented higher than that of the pure ZnIn_2S_4 (3.7%) or pure CaIn_2S_4 (2.3%). In addition, the AQE for the Cr(VI) reduction increased gradually with the increase of the CaIn_2S_4 constituent when the addition ratio of the CaIn_2S_4 precursor was no more than 30%. However, further increasing the molar ratio of CaIn_2S_4 led to a decrease in the AQE. This suggests that the heterostructured composites containing a suitable amount of CaIn_2S_4 and ZnIn_2S_4 contributed to improving optimally the photoactivity for the Cr(VI) reduction. Therefore, the optimal 30% $\text{CaIn}_2\text{S}_4/\text{ZnIn}_2\text{S}_4$ has been chosen as a representative catalyst for the following studies.

To further clarify the influence of the heterostructure on the photocatalytic performance of the Cr(VI) reduction, the 30% CaIn₂S₄/ZnIn₂S₄ sample was compared to its mechanical mixing counterpart sample 30% CaIn₂S₄ + 70% ZnIn₂S₄. The photocatalytic activity of the Cr(VI) reduction over the physical mixture was much lower than that of the 30% CaIn₂S₄/ZnIn₂S₄ composite obtained via the one-step hydrothermal method. This result shows that the heterojunction formed between the CaIn₂S₄ and ZnIn₂S₄ contributed to improving photocatalytic efficiency of the Cr(VI) reduction.

When using the optimal 30% CaIn₂S₄/ZnIn₂S₄ as a photocatalyst, the change in the temporal absorption spectra of the DPC-Cr(VI) complex solution is illustrated in Figure 6B. The absorption peak at 540 nm belonging to the DPC-Cr(VI) complex decreased rapidly with the increase of light irradiation time, and it almost vanished after light illumination for 30 min. To gain more insight into the photocatalytic process, the total Cr ions concentrations over the 30% CaIn₂S₄/ZnIn₂S₄ photocatalyst after the treated samples were measured by ICP emission spectrometer (Figure S1, Supplementary Materials). As indicated in Figure S1, the initial concentration of Cr(VI) is 19.6 ppm. The measured total Cr ions concentration after 30 min light irradiation were found to be 19.1 ppm. This result demonstrates that almost no Cr(0) was produced in the present photocatalytic system. That is to say, Cr(VI) was primarily reduced to Cr(III) by the photogenerated electrons of the CaIn₂S₄/ZnIn₂S₄ composites.

In addition, the photocatalytic experiments for the Cr(VI) reduction under different pH conditions with 30% CaIn₂S₄/ZnIn₂S₄ were also carried out, and the corresponding results are presented in Figure 6C. In a photocatalytic system, the reduction efficiency of the aqueous Cr(VI) was greatly influenced by the pH value according to the previous reports [30]. Cr(VI) existed in two forms in alkaline and acid medium, respectively. CrO₄²⁻ is predominant in the alkaline medium, whereas Cr₂O₇²⁻ plays a major role in the acid medium. The chemical redox reaction can be outlined as follows:



As depicted in Figure 6C, the reduction rate of Cr(VI) increased with the decrease of the pH value. About 38.7%, 58.8%, 80.6%, and 89.0% of Cr(VI) are reduced at pH 10, 8, 6, and 4 in the first 15 min, respectively. This could be due to the fact that the Cr(OH)₃ precipitate produced in the alkaline medium covers the activity sites of the photocatalysts [38]. The results demonstrate the acidic condition was more beneficial to the photocatalytic reduction of Cr(VI) over the synthesized CaIn₂S₄/ZnIn₂S₄ composites.

Additionally, the controlled experiment by adding K₂S₂O₈ (the trapping agent of photo-generated electrons, 0.1 mmol) [39] into the photocatalytic system of the Cr(VI) reduction was performed, and the corresponding result is depicted in Figure 6D. It can be seen clearly that the Cr(VI) reduction over the optimal photocatalyst 30% CaIn₂S₄/ZnIn₂S₄ hardly occurs in the presence of K₂S₂O₈, which indicates that the reduction of Cr(VI) is conducted by photogenerated electrons under simulated sunlight irradiation. These results also indicate that a suitable amount of CaIn₂S₄ can effectively improve the photocatalytic performance of ZnIn₂S₄ toward the Cr(VI) reduction.

3.5. Catalytic Stability

The stability of a given photocatalyst was also an important factor in the practical application [40]. Furthermore, narrow bandgap semiconductors are generally more unstable when exposed to the sunlight illumination [24]. To study the effect of the CaIn₂S₄/ZnIn₂S₄ heterostructure on the catalytic stability, the cycle experiments of the Cr(VI) reduction were carried out and compared by using ZnIn₂S₄ and 30% CaIn₂S₄/ZnIn₂S₄ as photocatalysts under simulated sunlight irradiation (Figure 7). The results indicate that for the pristine ZnIn₂S₄, the reduction efficiency of Cr(VI) decreased about 20.9% after five repeated uses, demonstrating that ZnIn₂S₄ was unstable to some extent under simulated sunlight illumination. In comparison, a relatively low decrease in the reduction efficiency of Cr(VI) over 30% CaIn₂S₄/ZnIn₂S₄ was observed, and only a ca. 2.6% decrease of the reduction

efficiency is obtained after reusing five cycles. This suggests that the sunlight stability of ZnIn_2S_4 can be improved through forming the heterojunction composites with CaIn_2S_4 . Additionally, the XPS analysis of the used 30% $\text{CaIn}_2\text{S}_4/\text{ZnIn}_2\text{S}_4$ catalyst was also performed, and the obtained results are displayed in Figure S2 of the Supplementary Materials. As can be found from Figure S2, the surface element composition and the chemical state of the 30% $\text{CaIn}_2\text{S}_4/\text{ZnIn}_2\text{S}_4$ sample before and after the photocatalytic reaction show no obvious difference. The results confirm the superior stability of the $\text{CaIn}_2\text{S}_4/\text{ZnIn}_2\text{S}_4$ composite photocatalysts under simulated sunlight, which is more promising for the practical photocatalytic applications in environmental restoration.

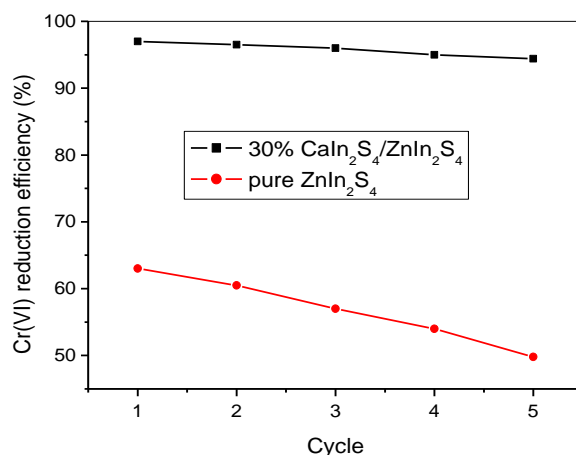


Figure 7. Photocatalytic stability tests of ZnIn_2S_4 and 30% $\text{CaIn}_2\text{S}_4/\text{ZnIn}_2\text{S}_4$ toward the Cr(VI) reduction.

3.6. Enhancement Mechanism of Photocatalytic Activity and Stability

On the basis of the above discussion and results, it is obvious that coupling a suitable amount of CaIn_2S_4 can dramatically improve the photocatalytic performance for the Cr(VI) reduction, including the reduction efficiency and cycling stability of the $\text{CaIn}_2\text{S}_4/\text{ZnIn}_2\text{S}_4$ composites. The remarkably enhanced photocatalytic activity of the $\text{CaIn}_2\text{S}_4/\text{ZnIn}_2\text{S}_4$ samples, compared with the pure CaIn_2S_4 and ZnIn_2S_4 , can be ascribed to the effective separation of the photogenerated electron/hole pairs due to the forming of flower-like heterostructures between ZnIn_2S_4 and CaIn_2S_4 . Generally, the photoluminescence spectrum (PLs) is considered as a vital technology to study the migration and fate of photoinduced charge carriers [39,41]. Higher intensities of PL signals usually represent higher recombination rates of photogenerated charge carriers, thus resulting in a lower photocatalytic performance. The comparison of the PL spectrum for the pristine ZnIn_2S_4 and 30% $\text{CaIn}_2\text{S}_4/\text{ZnIn}_2\text{S}_4$ with an excitation wavelength of 330 nm is presented in Figure 8. The pristine ZnIn_2S_4 showed emissions at 520, 571, and 656 nm. The strong emission peak centered at 520 nm for the pristine ZnIn_2S_4 was attributed to the intrinsic luminescence of ZnIn_2S_4 . The relatively weak PL peaks at 571, and 656 nm can be ascribed to the surface state emissions, which were mainly caused by the surface defects in the ZnIn_2S_4 structure. In comparison with the pristine ZnIn_2S_4 , there was no new emission signal in the PL spectrum of 30% $\text{CaIn}_2\text{S}_4/\text{ZnIn}_2\text{S}_4$, but the intensities of the PL peaks decreased obviously. The results imply that the photogenerated electrons and holes can transfer effectively between CaIn_2S_4 and ZnIn_2S_4 , thus suppressing the recombination of charge carriers. This can be a primary reason for the $\text{CaIn}_2\text{S}_4/\text{ZnIn}_2\text{S}_4$ composites possessing excellent photocatalytic reduction performance under simulated sunlight irradiation.

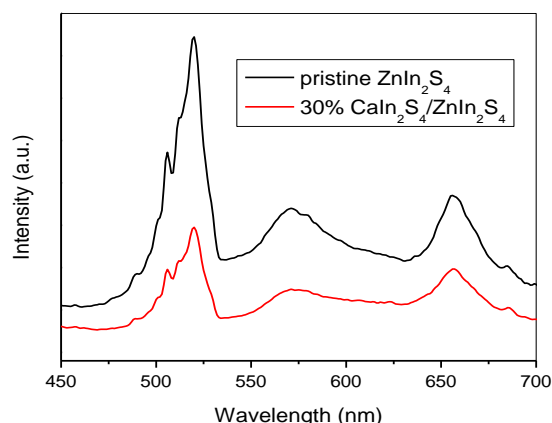


Figure 8. Room temperature photoluminescence spectra (PLs) of the pure ZnIn_2S_4 and 30% $\text{CaIn}_2\text{S}_4/\text{ZnIn}_2\text{S}_4$ under the excitation wavelength of 330 nm.

Most of the heterostructured nanocomposites follow the bidirectional charge transfer mechanism [42,43]. For instance, Kumar and his colleagues have reported on the photoinduced electrons enriched on the conduction band of Ag_3PO_4 and holes on the valence band of $g\text{-C}_3\text{N}_4$, which was conducted through a bidirectional charge transfer process between Ag_3PO_4 and $g\text{-C}_3\text{N}_4$ [42]. As for the as-prepared $\text{CaIn}_2\text{S}_4/\text{ZnIn}_2\text{S}_4$ composites, the aforementioned bidirectional charge transfer was also the primary charge migration process. Based on the bandgap energies of CaIn_2S_4 and ZnIn_2S_4 estimated from Figure 5 and Equations (2) and (3), the energy band structure diagram of CaIn_2S_4 and ZnIn_2S_4 can be schematically illustrated, as shown in Figure 9. Under light illumination, the components of CaIn_2S_4 and ZnIn_2S_4 were simultaneously excited, generating photoinduced electron/hole pairs. Due to the more negative conduction-band edge of CaIn_2S_4 (-1.12 eV) than that of ZnIn_2S_4 (-0.85 eV), the photogenerated electrons prefer to transfer from the CB of CaIn_2S_4 to ZnIn_2S_4 , whereas the photogenerated holes on the more positive VB of ZnIn_2S_4 ($+1.58$ eV) would migrate to that of CaIn_2S_4 ($+0.91$ eV). This bidirectional charge transfer process results in efficient separation of photogenerated electron/hole pairs in the synthesized $\text{CaIn}_2\text{S}_4/\text{ZnIn}_2\text{S}_4$ composites.

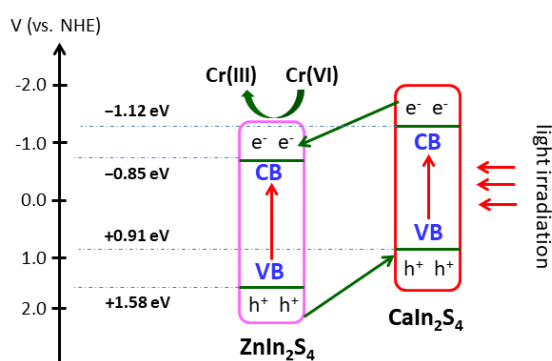


Figure 9. Schematic diagram of the transfer and separation of photogenerated charges in the $\text{CaIn}_2\text{S}_4/\text{ZnIn}_2\text{S}_4$ composites under simulated sunlight irradiation.

To further investigate the important function of heterostructures in enhancing the separation of charge carriers, the transient photocurrent responses were measured over working electrodes made of the pure CaIn_2S_4 , ZnIn_2S_4 , and 30% $\text{CaIn}_2\text{S}_4/\text{ZnIn}_2\text{S}_4$ composite. As depicted in Figure 10, the fast and steady photocurrent response can be detected for each light-on and light-off cycle over the pure CaIn_2S_4 , ZnIn_2S_4 , and 30% $\text{CaIn}_2\text{S}_4/\text{ZnIn}_2\text{S}_4$ composite. The pristine CaIn_2S_4 exhibited a very low photocurrent density, whereas the pure ZnIn_2S_4 showed a relatively higher photocurrent than that of

CaIn₂S₄ under simulated sunlight irradiation. This could be due to the fact that CaIn₂S₄ possesses a narrower bandgap than ZnIn₂S₄, which is unfavorable for the effective separation of photoinduced electron/hole pairs. This would result in the short survival time of photogenerated electrons and weak photocurrent density. However, the composite sample of 30% CaIn₂S₄/ZnIn₂S₄ exhibits a dramatically enhanced photocurrent density compared with that of the pure ZnIn₂S₄ and CaIn₂S₄, which further substantiates the efficient separation of the photoinduced electron/hole pairs in the obtained CaIn₂S₄/ZnIn₂S₄ composites.

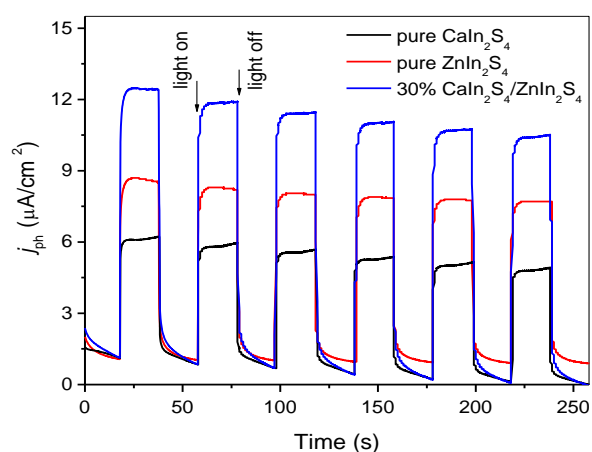


Figure 10. Photocurrent spectra of the as-synthesized pure CaIn₂S₄, ZnIn₂S₄, and 30% CaIn₂S₄/ZnIn₂S₄ samples under simulated sunlight irradiation with 20 s light on/off cycles.

Based on the above experimental results and the charge transfer process depicted in Figure 9, a possible enhancement mechanism of photocatalytic activity and stability for the Cr(VI) reduction can be proposed. Under simulated sunlight irradiation, the components of CaIn₂S₄ and ZnIn₂S₄ are excited to produce photoinduced holes and electrons. Owing to the relatively high recombination rate of photogenerated electron/hole pairs, the pristine CaIn₂S₄ and ZnIn₂S₄ exhibited low photocatalytic performance. Due to the well-matched energy band structures and the intimate interfacial contact between CaIn₂S₄ and ZnIn₂S₄ in the as-synthesized composites, the photoinduced electrons located on the CB of CaIn₂S₄ can easily migrate to that of ZnIn₂S₄, and on the contrary, the photoinduced holes on the VB of ZnIn₂S₄ spontaneously transfer to that of CaIn₂S₄ (Figure 9). These photoelectrons (e⁻) accumulated on the CB of ZnIn₂S₄ possess a strong reduction ability (−0.85 eV vs. NHE (normal hydrogen electrode)), which can reduce toxic Cr(VI) to Cr(III) ($E_{\text{Cr(VI)/Cr(III)}} = +0.55$ eV vs. NHE) [44,45]. The photoholes located on the VB of CaIn₂S₄ react with the sacrificial reagents immediately. The heterostructured composites formed between CaIn₂S₄ and ZnIn₂S₄ effectively prevent the recombination of photogenerated electrons and holes, and thus, the photocatalytic activities of the Cr(VI) reduction are enhanced greatly. Meanwhile, the effective transfer of photogenerated holes from the VB of ZnIn₂S₄ to that of CaIn₂S₄ is beneficial for preventing the oxidation of S²⁻ by holes, which significantly improves the photostability of ZnIn₂S₄ in the composite catalysts.

4. Conclusions

In short, the CaIn₂S₄/ZnIn₂S₄ composite photocatalysts were successfully prepared through a one-step hydrothermal process. XRD patterns show that the as-synthesized flower-like composites consist of hexagonal phase ZnIn₂S₄ and cubic phase CaIn₂S₄. Compared with the pristine ZnIn₂S₄, the heterostructured composites CaIn₂S₄/ZnIn₂S₄ show significantly improved photocatalytic activity and stability for the Cr(VI) reduction under simulated sunlight illumination. The molar content of CaIn₂S₄ has a great influence on the photocatalytic activity of the CaIn₂S₄/ZnIn₂S₄ composites, and 30% CaIn₂S₄/ZnIn₂S₄ exhibits the optimal photocatalytic performance for the Cr(VI) reduction.

A possible mechanism of the photogenerated charge transfer was proposed to illustrate the superior photocatalytic performance and photostability of the $\text{CaIn}_2\text{S}_4/\text{ZnIn}_2\text{S}_4$ composite catalysts. This study is of great importance in the design and synthesis of heterostructured sulfide composites with excellent photocatalytic performance and consistent stability toward the elimination of toxic metal ions in water.

Supplementary Materials: The following are available online at <http://www.mdpi.com/2079-4991/8/7/472/s1>, Figure S1: Concentrations of Cr(VI) and total Cr ions in the photocatalytic reaction solution over 30% $\text{CaIn}_2\text{S}_4/\text{ZnIn}_2\text{S}_4$ catalyst under simulated sunlight irradiation., Figure S2: XPS survey spectra (a), high-resolution XPS spectra of Zn 2p (b), In 3d (c), Ca 2p (d), and S 2p (e) of 30% $\text{CaIn}_2\text{S}_4/\text{ZnIn}_2\text{S}_4$ composite sample before and after the photocatalytic reaction, respectively.

Author Contributions: J.Y. (Juan Yang) proposed and planned the research and supervised the experiments. J.D. designed the synthesis of the photocatalysts. S.X. and J.Y. (Jun You) prepared the photocatalysts and performed the characterization and photocatalytic measurements. J.D. and J.H. improved the data analysis. All the authors collaborated and participated in writing of the manuscript.

Acknowledgments: This work has been supported by the National Nature Science Foundation of China (21307027), the Scientific and Technological Project of Henan Province (172102310725), the Funding Scheme for the Young Backbone Teachers of Higher Education Institutions in Henan Province (2015GGJS-071), the Fundamental Research Funds for the Universities of Henan Province (NSFRF170303), the Foundation for Distinguished Young Scientists (J2016-4), and the Innovative Research Team (T2018-2) of Henan Polytechnic University.

Conflicts of Interest: The authors declare no conflict of interest.

References

1. Yang, L.X.; Luo, S.L.; Li, Y.; Xiao, Y.; Kang, Q.; Cai, Q.Y. High efficient photocatalytic degradation of p-nitrophenol on a unique $\text{Cu}_2\text{O}/\text{TiO}_2$ p-n heterojunction network catalyst. *Environ. Sci. Technol.* **2010**, *44*, 7641–7646. [[CrossRef](#)] [[PubMed](#)]
2. Liu, Y.M.; Hou, C.L.; Jiao, T.F.; Song, J.W.; Zhang, X.; Xing, R.R.; Zhou, J.X.; Zhang, L.X.; Peng, Q.M. Self-assembled AgNP-containing nanocomposites constructed by electrospinning as efficient dye photocatalyst materials for wastewater treatment. *Nanomaterials* **2018**, *8*, 35. [[CrossRef](#)] [[PubMed](#)]
3. Wang, X.L.; Pehkonen, S.O.; Ray, A.K. Removal of aqueous Cr(VI) by a combination of photocatalytic reduction and coprecipitation. *Ind. Eng. Chem. Res.* **2004**, *43*, 1665–1672. [[CrossRef](#)]
4. Yin, H.B.; Wada, Y.; Kitamura, T.; Yanagida, S. Photoreductive dehalogenation of halogenated benzene derivatives using ZnS or CdS nanocrystallites as photocatalysts. *Environ. Sci. Technol.* **2001**, *35*, 227–231. [[CrossRef](#)] [[PubMed](#)]
5. Zhou, R.X.; Guzman, M.I. CO_2 reduction under periodic illumination of ZnS. *J. Phys. Chem. C* **2014**, *118*, 11649–11656. [[CrossRef](#)]
6. Zhou, R.X.; Guzman, M.I. Photocatalytic reduction of fumarate to succinate on ZnS mineral surfaces. *J. Phys. Chem. C* **2016**, *120*, 7349–7357. [[CrossRef](#)]
7. Baran, T.; Wojtyla, S.; Dibenedetto, A.; Aresta, M.; Macyk, W. Zinc sulfide functionalized with ruthenium nanoparticles for photocatalytic reduction of CO_2 . *Appl. Catal. B Environ.* **2015**, *178*, 170–176. [[CrossRef](#)]
8. Wojtyla, S.; Baran, T. Insight on doped ZnS and its activity towards photocatalytic removing of Cr(VI) from wastewater in the presence of organic pollutants. *Mater. Chem. Phys.* **2018**, *212*, 103–112. [[CrossRef](#)]
9. Wang, W.J.; Ng, T.W.; Ho, W.K.; Huang, J.H.; Liang, S.J.; An, T.C.; Li, G.Y.; Yu, J.C.; Wong, P.K. CdIn_2S_4 microsphere as an efficient visible-light-driven photocatalyst for bacterial inactivation: Synthesis, characterizations and photocatalytic inactivation mechanisms. *Appl. Catal. B Environ.* **2013**, *129*, 482–490. [[CrossRef](#)]
10. Tu, X.L.; Lu, J.; Li, M.; Su, Y.J.; Yin, G.L.; He, D.N. Hierarchically ZnIn_2S_4 nanosheet-constructed microwire arrays: Template-free synthesis and excellent photocatalytic performances. *Nanoscale* **2018**, *10*, 4735–4744. [[CrossRef](#)] [[PubMed](#)]
11. Gou, X.L.; Cheng, F.Y.; Shi, Y.H.; Zhang, L.; Peng, S.J.; Chen, J.; Shen, P.W. Shape-controlled synthesis of ternary chalcogenide ZnIn_2S_4 and $\text{CuIn}(\text{S},\text{Se})_2$ nano-/microstructures via facile solution route. *J. Am. Chem. Soc.* **2006**, *128*, 7222–7229. [[CrossRef](#)] [[PubMed](#)]
12. Li, L.L.; Peng, S.J.; Wang, N.; Srinivasan, M.; Mhaisalkar, S.G.; Yan, Q.Y.; Ramakrishna, S. A general strategy toward carbon cloth-based hierarchical films constructed by porous nanosheets for superior photocatalytic activity. *Small* **2015**, *11*, 2429–2436. [[CrossRef](#)] [[PubMed](#)]

13. Yu, X.; Shavel, A.; An, X.Q.; Luo, Z.S.; Ibáñez, M.; Cabot, A. Cu₂ZnSnS₄-Pt and Cu₂ZnSnS₄-Au heterostructured nanoparticles for photocatalytic water splitting and pollutant degradation. *J. Am. Chem. Soc.* **2014**, *136*, 9236–9239. [[CrossRef](#)] [[PubMed](#)]
14. Gao, B.; Liu, L.F.; Liu, J.D.; Yang, F.L. Photocatalytic degradation of 2,4,6-tribromophenol over Fe-doped ZnIn₂S₄: Stable activity and enhanced debromination. *Appl. Catal. B Environ.* **2013**, *129*, 89–97. [[CrossRef](#)]
15. Guan, Z.J.; Xu, Z.Q.; Li, Q.Y.; Wang, P.; Li, G.Q.; Yang, J.J. AgIn₅S₈ nanoparticles anchored on 2D layered ZnIn₂S₄ to form OD/2D heterojunction for enhanced visible-light photocatalytic hydrogen evolution. *Appl. Catal. B Environ.* **2018**, *227*, 512–518. [[CrossRef](#)]
16. Yuan, Y.J.; Chen, D.Q.; Zhong, J.S.; Yang, L.X.; Wang, J.J.; Liu, M.J.; Tu, W.G.; Yu, Z.T.; Zou, Z.G. Interface engineering of a noble-metal-free 2D-2D MoS₂/Cu-ZnIn₂S₄ photocatalyst for enhanced photocatalytic H₂ production. *J. Mater. Chem. A* **2017**, *5*, 15771–15779. [[CrossRef](#)]
17. Tan, C.W.; Zhu, G.Q.; Hojamberdiev, M.; Lokesh, K.S.; Luo, X.C.; Jin, L.; Zhou, J.P.; Liu, P. Adsorption and enhanced photocatalytic activity of the {0001} faceted Sm-doped ZnIn₂S₄ microspheres. *J. Hazard. Mater.* **2014**, *278*, 572–583. [[CrossRef](#)] [[PubMed](#)]
18. Xu, F.Y.; Zhang, J.J.; Zhu, B.C.; Yu, J.G.; Xu, J.S. CuInS₂ sensitized TiO₂ hybrid nanofibers for improved photocatalytic CO₂ reduction. *Appl. Catal. B Environ.* **2018**, *230*, 194–202. [[CrossRef](#)]
19. Aguirre, M.E.; Zhou, R.X.; Eugene, A.J.; Guzman, M.I.; Grela, M.A. Cu₂O/TiO₂ heterostructures for CO₂ reduction through a direct Z-scheme: Protecting Cu₂O from photocorrosion. *Appl. Catal. B Environ.* **2017**, *217*, 485–493. [[CrossRef](#)]
20. Wu, Z.; Gong, C.; Yu, J.; Sun, L.; Xiao, W.; Lin, C. Enhanced visible light photoelectrocatalytic activity over Cu_xZn_{1-x}In₂S₄@TiO₂ nanotube array hetero-structures. *J. Mater. Chem. A* **2017**, *5*, 1292–1299. [[CrossRef](#)]
21. Hou, J.; Yang, C.; Cheng, H.; Wang, Z.; Jiao, S.; Zhu, H. Ternary 3D architectures of CdS QDs/graphene/ZnIn₂S₄ heterostructures for efficient photocatalytic H₂ production. *Phys. Chem. Chem. Phys.* **2013**, *15*, 15660–15668. [[CrossRef](#)] [[PubMed](#)]
22. Zhang, Z.; Liu, K.; Feng, Z.; Bao, Y.; Dong, B. Hierarchical sheet-on-sheet ZnIn₂S₄/g-C₃N₄ heterostructure with highly efficient photocatalytic H₂ production based on photoinduced interfacial charge transfer. *Sci. Rep.* **2016**, *6*, 19221. [[CrossRef](#)] [[PubMed](#)]
23. Huang, S.; Lin, Y.; Yang, J.H.; Yu, Y. CdS-based semiconductor photocatalysts for hydrogen production from water splitting under solar light. *ACS Symp. Ser.* **2013**, *1140*, 219–241. [[CrossRef](#)]
24. Chen, J.Y.; Zhang, H.M.; Liu, P.R.; Li, Y.B.; Liu, X.L.; Li, G.Y.; Wong, P.K.; An, T.C.; Zhao, H.J. Cross-linked ZnIn₂S₄/rGO composite photocatalyst for sunlight-driven photocatalytic degradation of 4-nitrophenol. *Appl. Catal. B Environ.* **2015**, *168–169*, 266–273. [[CrossRef](#)]
25. Yuan, W.H.; Yang, S.; Li, L. Synthesis of g-C₃N₄/CaIn₂S₄ composites with enhanced photocatalytic activity under visible light irradiation. *Dalton Trans.* **2015**, *44*, 16091–16098. [[CrossRef](#)] [[PubMed](#)]
26. Ding, J.J.; Yan, W.H.; Sun, S.; Bao, J.; Gao, C. Hydrothermal synthesis of CaIn₂S₄-reduced graphene oxide nanocomposites with increased photocatalytic performance. *ACS Appl. Mater. Interfance* **2014**, *6*, 12877–12884. [[CrossRef](#)] [[PubMed](#)]
27. Jo, W.K.; Natarajan, T.S. Facile synthesis of novel redox-mediator-free direct Z-Scheme CaIn₂S₄ marigold-flower-like/TiO₂ photocatalysts with superior photocatalytic efficiency. *ACS Appl. Mater. Interfance* **2015**, *7*, 17138–17154. [[CrossRef](#)] [[PubMed](#)]
28. Testa, J.J.; Grela, M.A.; Litter, M.I. Heterogeneous photocatalytic reduction of chromium(VI) over TiO₂ particles in the presence of oxalate: Involvement of Cr(V) species. *Environ. Sci. Technol.* **2004**, *38*, 1589–1594. [[CrossRef](#)] [[PubMed](#)]
29. Fu, F.L.; Wang, Q. Removal of heavy metal ions from wastewaters: A review. *J. Environ. Manag.* **2011**, *92*, 407–418. [[CrossRef](#)] [[PubMed](#)]
30. Liu, F.H.; Yu, J.; Tu, G.Y.; Qu, L.; Xiao, J.C.; Liu, Y.D.; Wang, L.Z.; Lei, J.Y.; Zhang, J.L. Carbon nitride coupled Ti-SBA15 catalyst for visible-light-driven photocatalytic reduction of Cr(VI) and the synergistic oxidation of phenol. *Appl. Catal. B Environ.* **2017**, *201*, 1–11. [[CrossRef](#)]
31. Nayak, A.K.; Lee, S.; Choi, Y.I.; Yoon, H.J.; Sohn, Y.; Pradhan, D. Crystal phase and size-controlled synthesis of tungsten trioxide hydrate nanoplates at room temperature: Enhanced Cr(VI) photoreduction and methylene blue adsorption properties. *ACS Sustain. Chem. Eng.* **2017**, *5*, 2741–2750. [[CrossRef](#)]

32. Yang, J.; You, J.; Dai, J.; Chen, Y.M.; Li, Y. In-situ synthesis of hydrogen-titanate nanotubes/graphene composites with chemically bonded interface and enhanced visible photocatalytic activity. *Nanomaterials* **2018**, *8*, 229. [[CrossRef](#)] [[PubMed](#)]
33. Wang, L.; Zhang, C.B.; Gao, F.; Mailhot, G.; Pan, G. Algae decorated TiO₂/Ag hybrid nanofiber membrane with enhanced photocatalytic activity for Cr(VI) removal under visible light. *Chem. Eng. J.* **2017**, *314*, 622–630. [[CrossRef](#)]
34. Ye, L.; Fu, J.L.; Xu, Z.; Yuan, R.S.; Li, Z.H. Facile one-pot solvothermal method to synthesize sheet-on-sheet reduced graphene oxide (RGO)/ZnIn₂S₄ nanocomposites with superior photocatalytic performance. *ACS Appl. Mater. Interfaces* **2014**, *6*, 3483–3490. [[CrossRef](#)] [[PubMed](#)]
35. Ding, J.; Sun, S.; Yan, W.; Bao, J.; Gao, C. Photocatalytic H₂ evolution on a novel CaIn₂S₄ photocatalyst under visible light irradiation. *Int. J. Hydrogen Energy* **2013**, *38*, 13153–13158. [[CrossRef](#)]
36. Zhang, X.; Zhang, J.; Yu, J.Q.; Zhang, Y.; Cui, Z.X.; Sun, Y.; Hou, B.R. Fabrication of InVO₄/AgVO₃ heterojunctions with enhanced photocatalytic antifouling efficiency under visible-light. *Appl. Catal. B Environ.* **2018**, *220*, 57–66. [[CrossRef](#)]
37. Shi, L.; Yin, P.Q.; Dai, Y.M. Synthesis and photocatalytic performance of ZnIn₂S₄ nanotubes and nanowires. *Langmuir* **2013**, *29*, 12818–12822. [[CrossRef](#)] [[PubMed](#)]
38. Deng, Y.C.; Tang, L.; Zeng, G.M.; Zhu, Z.J.; Yan, M.; Zhou, Y.Y.; Wang, J.J.; Liu, Y.N.; Wang, J.J. Insight into highly efficient simultaneous photocatalytic removal of Cr(VI) and 2,4-dichlorophenol under visible light irradiation by phosphorus doped porous ultrathin g-C₃N₄ nanosheets from aqueous media: Performance and reaction mechanism. *Appl. Catal. B Environ.* **2017**, *203*, 343–354. [[CrossRef](#)]
39. Liu, S.Q.; Yang, M.Q.; Tang, Z.R.; Xu, Y.J. A nanotree-like CdS/ZnO nanocomposite with spatially branched hierarchical structure for photocatalytic fine-chemical synthesis. *Nanoscale* **2014**, *6*, 7193–7198. [[CrossRef](#)] [[PubMed](#)]
40. Gilja, V.; Novakovic, K.; Travas-Sejdic, J.; Hrnjak-Murgic, Z.; Rokovic, M.K.; Zic, M. Stability and synergistic effect of polyaniline/TiO₂ photocatalysts in degradation of Azo dye in wastewater. *Nanomaterials* **2017**, *7*, 412. [[CrossRef](#)] [[PubMed](#)]
41. Wu, N.; Wang, J.; Tafen, D.N.; Wang, H.; Zheng, J.-G.; Lewis, J.P.; Liu, X.; Leonard, S.S.; Manivannan, A. Shape-enhanced photocatalytic activity of single-crystalline anatase TiO₂ (101) nanobelts. *J. Am. Chem. Soc.* **2010**, *132*, 6679–6685. [[CrossRef](#)] [[PubMed](#)]
42. Kumar, S.; Surendar, T.; Baruah, A.; Shanker, V. Synthesis of a novel and stable g-C₃N₄-Ag₃PO₄ hybrid nanocomposite photocatalyst and study of the photocatalytic activity under visible light irradiation. *J. Mater. Chem. A* **2013**, *1*, 5333–5340. [[CrossRef](#)]
43. Xiong, P.; Zhu, J.W.; Wang, X. Cadmium sulfide-ferrite nanocomposite as a magnetically recyclable photocatalyst with enhanced visible-light-driven photocatalytic activity and photostability. *Ind. Eng. Chem. Res.* **2013**, *52*, 17126–17133. [[CrossRef](#)]
44. Qiu, J.H.; Zhang, X.F.; Zhang, X.G.; Feng, Y.; Li, Y.X.; Yang, L.Y.; Lu, H.Q.; Yao, J.F. Constructing Cd_{0.5}Zn_{0.5}S@ZIF-8 nanocomposites through self-assembly strategy to enhance Cr(VI) photocatalytic reduction. *J. Hazard. Mater.* **2018**, *349*, 234–241. [[CrossRef](#)] [[PubMed](#)]
45. Yuan, Y.J.; Chen, D.Q.; Shi, X.F.; Tu, J.R.; Hu, B.; Yang, L.X.; Yu, Z.T.; Zou, Z.G. Facile fabrication of “green” SnS₂ quantum dots/reduced graphene oxide composites with enhanced photocatalytic performance. *Chem. Eng. J.* **2017**, *313*, 1438–1446. [[CrossRef](#)]

